Biobased Photopolymer Resin for 3D Printing Containing Dynamic Imine Bonds for Fast Reprocessability

Stouten, Jules; Schnelting, Geraldine H.M.; Hul, Jerzy; Sijstermans, Nick; Janssen, Kylian; Darikwa, Tinashe; Ye, Chongnan; Loos, Katja; Voet, Vincent S.D.; Bernaerts, Katrien V.

Published in:
ACS Applied Materials and Interfaces

DOI:
10.1021/acsami.3c01669

Publication date:
2023

Letter

Long-distance magnon transport in the van der Waals antiferromagnet $CrPS_4$

Dennis K. de Wal,[1,*] Arnaud Iwens,[1] Tian Liu,[1] Ping Tang,[2] Gerrit E. W. Bauer,[1,2,3] and Bart J. van Wees[1]

[1]*Zernike Institute for Advanced Materials, University of Groningen, Groningen, The Netherlands*

[2]*Advanced Institute for Materials Research (AIMR), Tohoku University, Sendai, Japan*

[3]*Kavli Institute for Theoretical Sciences, University of the Chinese Academy of Sciences, Beijing, China*

(Received 2 December 2022; revised 14 April 2023; accepted 19 April 2023; published 11 May 2023)

We demonstrate the potential of van der Waals magnets for spintronic applications by reporting long-distance magnon spin transport in the electrically insulating antiferromagnet chromium thiophosphate ($CrPS_4$) with perpendicular magnetic anisotropy. We inject and detect magnon spins nonlocally by Pt contacts and monitor the nonlocal resistance as a function of an in-plane magnetic field up to 7 T. We observe a nonlocal resistance over distances up to at least a micron below the Néel temperature ($T_N = 38$ K) close to magnetic field strengths that saturate the sublattice magnetizations.

DOI: 10.1103/PhysRevB.107.L180403

Since the discovery of the long-range magnetic order in mono- and bilayers of $Cr_2Ge_2Te_6$ [1] and CrI_3 [2] many (anti)ferromagnetic van der Waals materials have been identified in monolayer or few-layer thicknesses. They are attractive platforms for spintronics due to the rich spin textures caused by the interplay of inter- and intralayer exchange and magnetic anisotropies.

Many antiferromagnetic van der Waals materials are electrically insulating at low temperatures, which implies the absence of magnetization damping by free carriers. They are therefore attractive for the study of collective excitations of the magnetic order, i.e., spin waves and its quanta, the magnons [3,4]. Magnon transport has been extensively studied in conventional magnets by, e.g., spin pumping [5], the spin Seebeck effect (SSE) [6], and electrical magnon spin injection/detection [7]. Long-distance magnon transport has been demonstrated in $YFeO_3$ [8] and in the antiferromagnets nickel oxide [9] and hematite [10], as well as coherent control of spin currents and magnon spin dynamics in the latter [11]. Ultrathin films of the low-damping ferrimagnetic yttrium iron garnet (YIG), the material of choice for efficient magnon transport, show the beneficial effects of two-dimensional (2D) vs three-dimensional (3D) transport in the form of strongly enhanced magnon conductivities [12]. Magnon spin transport driven by temperature gradients (SSE) [13] has been reported in ferro- and antiferromagnetic van der Waals materials [14,15]. However, the local and nonlocal SSEs provide only convoluted information on the magnon transport properties. Thermal magnon currents are generated by thermal gradients in the entire sample, making it difficult to disentangle the magnon relaxation length and magnon spin conductivity [7,12]. Antiferromagnetic resonance of $CrCl_3$ [16] reveals the existence of acoustic and optical magnon modes, but does not resolve their roles in spin transport. In order to assess the potential of van der Waals magnets for spintronic applications, we therefore have to study the propagation of magnons that are locally generated by microwaves or, as we will show here, by electrical injection.

Heavy metal contacts such as Pt with a large (inverse) spin Hall effect have become a standard instrument to study magnetic materials. The spin Hall magnetoresistance (SMR) in a Pt contact is a reliable method to measure the surface equilibrium magnetization [17], which has already been used to study $CrPS_4$ [18] and $FePS_3$ [19]. With two Pt contacts, the spins injected by an electric current in one terminal by the spin Hall effect propagate in an electrically insulating magnet in the form of magnons, which can be detected by another contact via the inverse spin Hall effect [7]. Here we report nonlocal "all-electrical" measurements of magnon transport in a van der Waals antiferromagnet, in our case $CrPS_4$.

$CrPS_4$ is an A-type antiferromagnet [see Fig. 1(a)]. Individual layers are out-of-plane (OOP) 2D ferromagnets, but consecutive layers order antiferromagnetically at a Néel temperature $T_N \simeq 38$ K. Its relative stability in air facilitates the fabrication of devices. An OOP field of $H_{\text{spin-flop}} \approx 0.9$ T (at 5 K) induces a spin-flop transition to a canted state, while the magnetization becomes saturated into a "spin-flip" state at 8.5 T. In-plane (IP) fields result in magnetization saturation at nearly the same field, indicating that the anisotropy field ($H_A \approx 0.01$ T) is much smaller than the exchange field ($H_E \approx 4.25$ T) [20,21]. $CrPS_4$ is therefore an excellent platform to study magnons in controlled noncollinear spin textures because the moderate spin-flop and spin-flip critical fields are accessible by standard laboratory equipment.

Figure 1(b) shows the calculated band-edge ($k = 0$) frequencies of the acoustic and optical magnons of a bilayer of $CrPS_4$ with easy axis along z as a function of IP magnetic fields using the parameters above. Figure 1(c) sketches the magnetization precession amplitudes for fields normal to the layers below the spin-flop transition ($H < H_{\text{spin-flop}}$) in which the Néel vector remains along z and the magnon modes carry opposite spins $+\hbar/-\hbar$, in the z direction. Figure 1(d) sketches the excitations of the canted spin texture at an IP magnetic

*d.k.de.wal@rug.nl

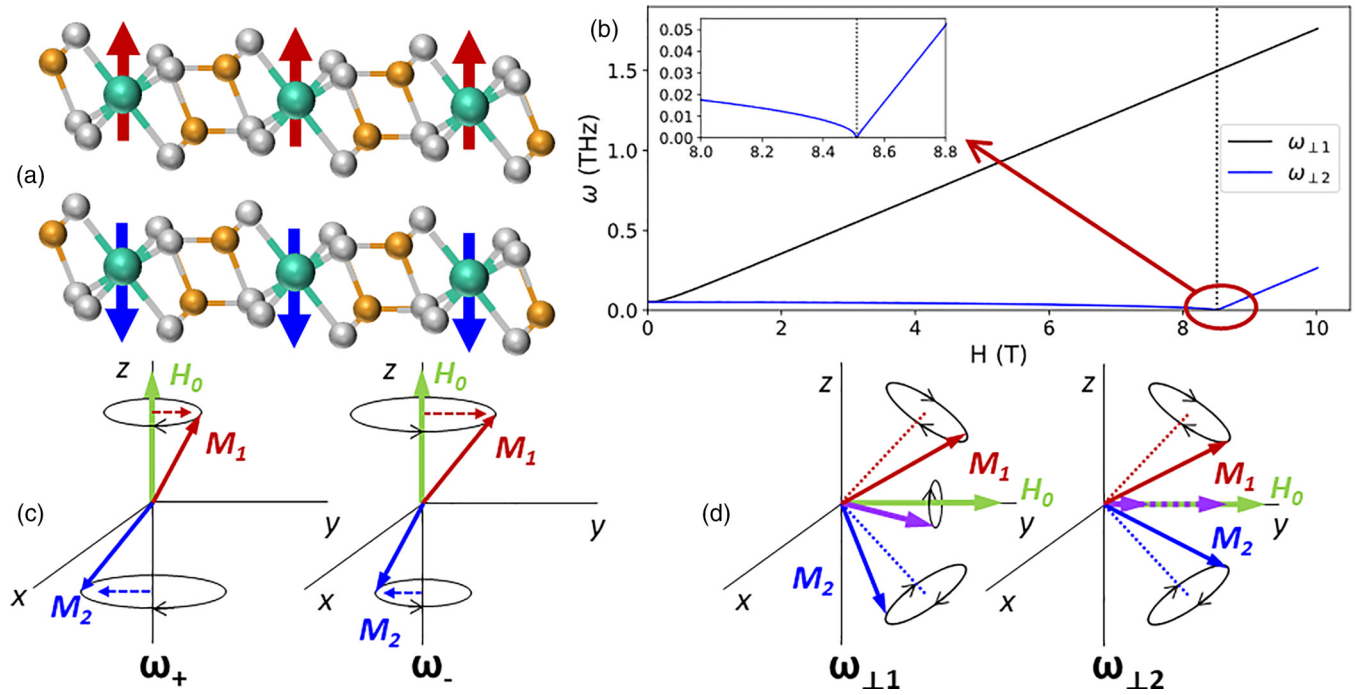

FIG. 1. Spin texture and magnon modes in antiferromagnetic $CrPS_4$. (a) Atom and spins of a bilayer of $CrPS_4$. Red and blue arrows indicate the local magnetic moments of the Cr atoms (turquoise). The interlayer (intralayer) exchange coupling is ferromagnetic (antiferromagnetic). (b) In-plane magnetic field dependence of the magnon band edges. (c) Optical (ω_+) and acoustic magnon modes at out-of-plane (OOP) magnetic fields below the spin-flop transition (d) magnon modes at in-plane (IP) magnetic fields below the spin-flip transition ($H < H_{E\perp}$). The net magnetization of the $\omega_{\perp 1}$ mode precesses (purple vector) around the IP external field vector with equal modulus, while that of the $\omega_{\perp 2}$ mode oscillates in the direction of the field.

field below the spin-flip transition ($H < H_{E\perp}$). The associated magnons evolve from the zero-field spin-up and spin-down states with a net magnetization along y as indicated by the purple arrows.

We fabricated three devices by depositing multiple parallel Pt strips on exfoliated $CrPS_4$ flakes with a thickness of ~100 nm [see Fig. 2(a)]. We study both the local and nonlocal resistances as a function of magnitude and direction of an IP magnetic field. We measure the magnetoresistance of a single Pt strip (SMR) [17] as well as magnon transport and the spin Seebeck effect nonlocally by two Pt strips [see Fig. 2(b)].

Via the SMR we monitor the surface magnetization as a function of temperature, IP external field, and bias current.

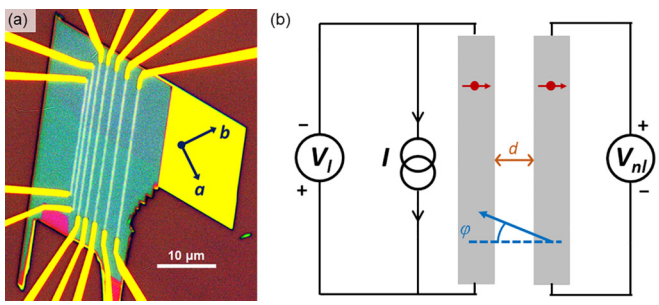

FIG. 2. (a) Optical micrograph of a transport device with seven parallel Pt strips bonded by Ti/Au leads on top of $CrPS_4$ film, where a and b indicate the orientation.of the single crystal. (b) Electrical measurement circuit, in which the red arrows indicate electrically active spins in the Pt strips and φ is an IP magnetic field angle.

The current I in a Pt strip generates a transverse spin current that when partially reflected at the Pt|$CrPS_4$ interface induces an additional current by the inverse spin Hall effect, effectively reducing the electrical resistance. A polarization of the spin Hall spin current [red arrows in Fig. 2(b)] parallel (normal) to the local moments of the magnet at the interface, minimizes (maximizes) the dephasing by the exchange interaction and therefore the electric resistance [17]. An in-plane magnetic field $\mathbf{H} = H\hat{\mathbf{y}}$ (IP angle $\varphi = 0$) cants the OOP antiferromagnetic order by an angle

$$\theta_\perp = \arcsin \frac{H}{2H_E + H_A} \tag{1}$$

with the z axis. The electric resistance R_l of a Pt wire along the x axis therefore should be maximal for $\theta_\perp = 0$ and minimal for $\theta_\perp = \pi/2$, i.e., at and beyond the spin-flip transition. On the other hand, magnon injection is most efficient when magnetic moments and current-induced spins are parallel, maximizing the nonlocal resistance $R_{nl} = V_{\text{detector}}/I_{\text{injector}}$. $R_{nl} > 0$ by defining the polarity of the voltage on the detector opposite to that of the current in the injector [see Fig. 2(b)].

The Joule heating by a charge current I generates a temperature gradient over the interface and in the magnet, generating a spin current and associated inverse spinHall voltage (spin Seebeck effect) in the injector as well as the detector with associated local and nonlocal voltage signals.

We can separate the electrical and thermal signals by recording the first and second harmonic responses to a current bias that oscillates with frequency ω. The first harmonic response reflects the Ohmic signal $V \sim I$, while the thermal

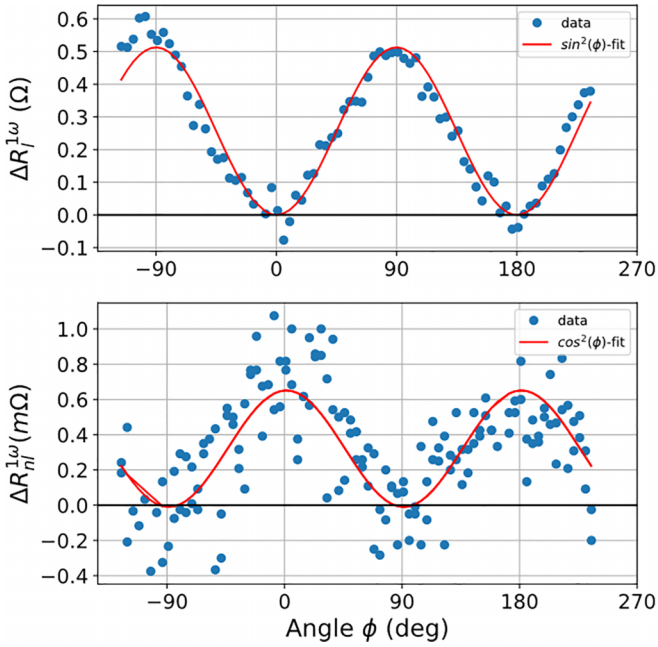

FIG. 3. Top panel: Local resistance modulation $\Delta R_l^{(1\omega)}$ of the Pt strip as function of in-plane angle φ (relative to the wire normal) of an applied magnetic field of 7 T. The bias current is 60 μA and sample temperature is 24 K. The red curve is a fit by $\sin^2\varphi$. A 5.97 kΩ offset resistance has been subtracted. Bottom panel: Simultaneously measured nonlocal resistance $R_{nl}^{(1\omega)}$, fitted by $\cos^2\varphi$ (red curve).

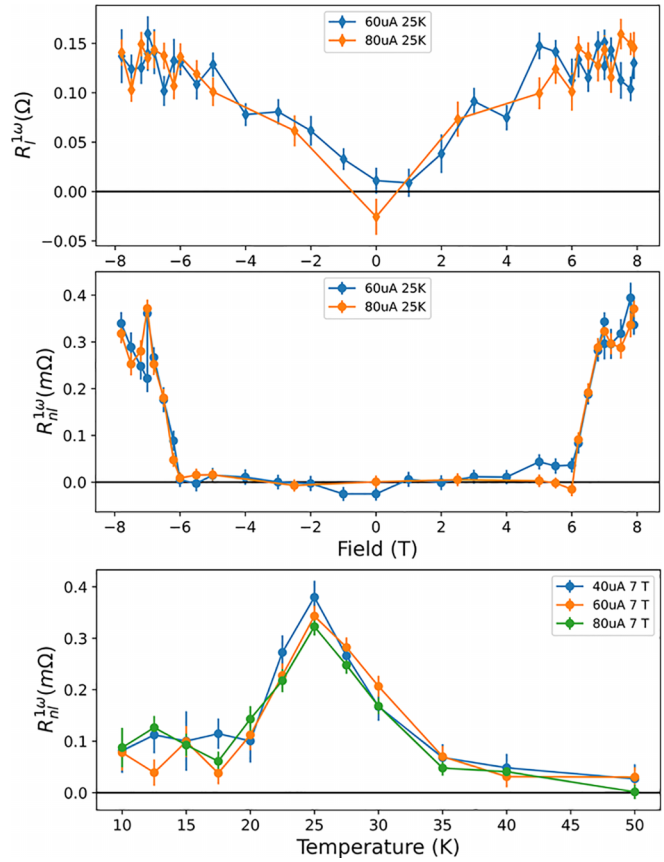

FIG. 4. Field- and temperature-dependent results on device D2. Top: Field dependence of $R_l^{1\omega}$ at different bias currents at 25 K. Middle: Same for $R_{nl}^{1\omega}$. Bottom: Temperature dependence of $R_{nl}^{1\omega}$ at 7 T.

signals $V \sim I^2$ appear at double frequency. Here we focus on the linear response $R_{l/nl}^{(1\omega)}$, with a brief discussion of $R_{l/nl}^{(2\omega)}$ in the Supplemental Material (SM) [22] (see also Ref. [23] therein). The spin Hall effect and inverse spin Hall effect dictate the following dependence on the IP field angle:

$$R_l^{(1\omega)} = R_{l,0}^{(1\omega)} + \Delta R_l^{(1\omega)} \sin^2\varphi, \tag{2}$$

$$R_{nl}^{(1\omega)} = \Delta R_{nl}^{(1\omega)} \cos^2\varphi, \tag{3}$$

where $R_{0,l/nl}^{(1\omega)}$ are constant offsets and $\Delta R_{l/nl}^{(1\omega)}$ are the strengths of the signals that depend on the IP field angle φ (defined in Fig. 2).

We measured the local and nonlocal resistance in a liquid-He cryostat at temperatures between 5 and 300 K as a function of an IP magnetic field up to 7.9 T and as a function of IP angle φ. Figure 2 shows the schematics of device D1 and the local and nonlocal measurement configurations. The measurements on D1 were carried out on three different pairs of Pt contacts with edge-to-edge distances of 330, 420, and 780 nm. On device D2, we measured the resistances for two different pairs (∼300 and ∼450 nm) of Pt contacts. Results for device D3 with similar flake thickness and contacts with an edge-to-edge spacing of 300 nm are shown in the SM [22].

The time-dependent voltage responses may be expanded as $V(t) = R_1 I(t) + R_2 I^2(t) + \cdots$, where standard low-frequency (7–17 Hz) lock-in techniques access the constants R_1 and R_2 [7,24].

Figure 3 shows the observed $R_l^{(1\omega)} - R_{l,0}^{(1\omega)} (\approx 6\ \mathrm{k\Omega})$ of the injector contact as a function of the direction of an IP magnetic field of 7 T at AC current bias of 60 μA and at $T = 24$ K. The observed φ dependence agrees well with the model for the SMR sketched above. $\Delta R_l^{(1\omega)}/R_{l,0}^{(1\omega)} \simeq 10^{-4}$ is of the same order of magnitude as the SMR of $CrPS_4$ in the OOP configuration [18] and that of other magnetic materials, which is a strong indication of an efficient interface exchange coupling and a large spin-mixing conductance.

The modulation $\Delta R_l^{(1\omega)}$ at $T = 20$ K in Fig. 4(a) as a function of magnetic field strength agrees also with expectations, while the lack of a bias-current dependence confirms that we are in the linear response regime. We observe saturation at fields > 6 T (see Fig. 4), which corresponds to the onset of the spin-flip state.

At fields of several tesla, the SMR decreases with temperature but persists above T_N and even up to room temperature (not shown), which is consistent with reports for $CrPS_4$ [18] and the van der Waals material $Cr_2Ge_2Te_6$ [25]. The robust SMR can possibly be ascribed to a T_N that is enhanced by the interface spin-orbit coupling and/or a paramagnetic SMR by a field-induced magnetization [26].

We now focus on the nonlocal signal $R_{nl}^{(1\omega)}$ plotted in the lower panel of Fig. 3 for current bias of 60 μA, $H = 7$ T, $T = 24$ K (measured together with $R_l^{(1\omega)}$). $\Delta R_l^{(1\omega)} \simeq 0.6$ mΩ is about 30 times smaller than that of Pt|YIG (thickness of 200 nm) [7]. $R_{nl}^{(1\omega)}$ is maximum (minimum) at $\phi = 0^\circ$ ($\phi = 90^\circ$) which reflects the angular dependence of the spin

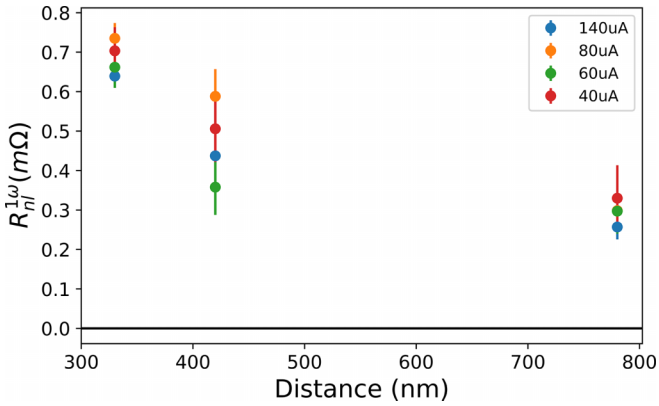

FIG. 5. Nonlocal resistance as a function of distance d between the injector and detector contacts. For different bias currents at sample temperature of 24 K, $R_{nl}^{(1\omega)} \sim 1/d$ is shown for three different Pt strip pairs on device D1 with d being equal to 330, 420, and 780 nm, respectively.

injection and detection efficiencies by the spin Hall effects in Pt.

Figure 4 reveals a remarkable dependence of the magnon transport on magnetic field. At $H \leqslant 6$ T, no $R_{nl}^{(1\omega)}$ is observed within the experimental uncertainty. At fields >6 T, $R_{nl}^{(1\omega)}$ increases sharply and appears to saturate at fields >7 T. This rapid increase correlates with the saturation of the bulk magnetization (see SM [22]) and is therefore associated with the spin-flip transition from a canted antiferromagnetic (AFM) to a collinear ferromagnetic (FM) state [see Figs. 1(c) and 1(d)].

The nonlocal resistance at current bias of 60 μA and at 7 T in Fig. 4 is nonmonotonous, with a maximum around 25 K. We attribute this to two effects. On one hand, the critical fields for the spin-flip transition decreases with temperature. At low temperatures and 7 T, the sample is still in the canted-AFM phase. The sharp increase in $R_{nl}^{(1\omega)}$ coincides with the formation of the saturated FM phase at $T \sim 25$ K. Moreover, the equilibrium magnon density and resulting magnon conductivity increase with temperature [27,28]. At larger temperatures, the magnetization and $R_{nl}^{(1\omega)}$ decrease and vanish at T_N.

Further, we assess the magnon transport in $CrPS_4$ by measuring as a function of distance d between the Pt contacts as shown in Fig. 5. The absence of a systematic dependence on the current bias again confirms that we operate in the linear response regime. The model of diffusive magnon transport in YIG leads to a decay of $R_{nl}^{(1\omega)}$ with increasing d as a function of the magnon diffusion length λ. For efficient spin injection at the Pt|YIG interface, this is described by [7]

$$R_{nl}^{(1\omega)} = \frac{C}{\lambda} \frac{\exp(d/\lambda)}{1-\exp(2d/\lambda)}, \tag{4}$$

where C is a constant. Since we observe an algebraic $R_{nl}^{(1\omega)} \sim 1/d$ rather than exponential dependence, magnon transport over the length scales $d \leqslant 1$ μm is Ohmic [7], i.e., purely diffusive while magnon decay sets in at larger distances only.

The abrupt field dependence of the nonlocal resistance differs sharply from the linear dependence of the SMR (top panel of Fig. 4) that indicates a surface magnetization proportional to a static magnetic susceptibility. A surprise of the present study is the absence of nonlocal transport in the noncollinear phase. This behavior is markedly different from previous studies of transport that were carried out with magnetic fields parallel to the Néel vector, including the spin-flop transition [8–10]. However, the associated theories do not address the present configuration either.

The magnon band edges of $CrPS_4$ in the canted phase as plotted in Fig. 1(b) diagonalize the classical spin Hamiltonian with eigenfrequencies [29] at low fields $H \leqslant H_{E\perp} = 2H_E + H_A$,

$$\begin{aligned}\omega_+ &= \gamma\sqrt{(2H_E\sin^2\theta_\perp + H_A\cos^2\theta_\perp)(2H_E+H_A)},\\ \omega_- &= \gamma\sqrt{H_A(2H_E+H_A)\cos^2\theta_\perp},\end{aligned} \tag{5}$$

and at high fields $H > H_{E\perp} = 2H_E + H_A$,

$$\begin{aligned}\omega_+ &= \gamma\sqrt{(H-H_A)H},\\ \omega_- &= \gamma\sqrt{(H-2H_E)(H-2H_E-H_A)},\end{aligned} \tag{6}$$

where $\theta_\perp$ is defined in Eq. (1) and includes the external IP field H. The small anisotropy causes the low frequencies of the acoustic modes that at high magnetic fields and low temperatures are dominantly populated.

The collinear ferromagnetic phase above $H_{E\perp}$ can be treated by a two-mode linearized Boltzmann equation similar to YIG, while the large SMR implies that interfaces are transparent. We may expect high nonlocal signals at $H > H_{E\perp}$. As the Pt contacts do not inject or detect spin polarizations in the z direction, i.e. at zero canting angle ($\theta_\perp$), the spin current injected by the Pt contacts is fully absorbed by the antiferromagnet in the form of a spin transfer torque to the magnetic sublattices, while magnon injection and $R_{nl}^{(1\omega)}$ vanish. With increasing canting angle, the magnon injection efficiency increases proportional with the induced net magnetization. However, the exchange interaction in a noncollinear configuration also increasingly affects the nonlocal signal by reducing the magnon decay length. Without detailed calculation the broken axial symmetry in the canted state allows magnon interband scattering processes that are symmetry forbidden in collinear magnets and dominated by the strong exchange interaction [30]. In the collinear phase both magnon injection and magnon transport do not prevent the nonlocal signal. The abruptness of the observed onset of nonlocal transport at the spin-flip transition field is surprising, however. The abrupt increase of nonlocal resistance near the spin-flip transition may be caused by the combined effects of enhanced magnon injection into the low-energy magnon branch and the sudden suppression of magnon relaxation when the system approaches the FM state.

Summarizing, we report nonlocal spin transport in a van der Waals magnet. The spin conduit is the electrically insulating antiferromagnet $CrPS_4$ with perpendicular anisotropy. We focus on a configuration that has escaped attention even in conventional antiferromagnets, with an in-plane magnetic field normal to the Pt spin injector and detector that tilts the antiparallel spins into the plane. Surprisingly, we do not observe spin transport in the noncollinear phase. At the critical field that forces the transition to a collinear ferromagnetic phase, we observe an abrupt increase of the nonlocal spin

signal over distances that exceed a micron. These results herald the potential of 2D van der Waals magnets for scalable magnonic circuits.

We acknowledge the technical support from J. G. Holstein, H. Adema, T. Schouten, H. H. de Vries, and F. H. van der Velde. We acknowledge the financial support of the Zernike Institute for Advanced Materials and the European Union's Horizon 2020 research and innovation program under Grant Agreements No. 785219 and No. 881603 (Graphene Flagship Core 2 and Core 3). This project is also financed by the NWO Spinoza prize awarded to B.J.W. by the NWO and has received funding from the European Research Council (ERC) under the European Union's 2DMAGSPIN (Grant Agreement No. 101053054). G.B. acknowledges funding by JSPS KAKENHI Grant No. 19H00645.

[1] C. Gong, L. Li, Z. Li, H. Ji, A. Stern, Y. Xia, T. Cao, W. Bao, C. Wang, Y. Wang, Z. Q. Qiu, R. J. Cava, S. G. Louie, J. Xia, and X. Zhang, Nature (London) **546**, 265 (2017).

[2] B. Huang, G. Clark, E. Navarro-Moratalla, D. R. Klein, R. Cheng, K. L. Seyler, D. Zhong, E. Schmidgall, M. A. McGuire, D. H. Cobden, W. Yao, D. Xiao, P. Jarillo-Herrero, and X. Xu, Nature (London) **546**, 270 (2017).

[3] F. Bloch, Z. Phys. **61**, 206 (1930).

[4] C. Kittel, *Introduction to Solid State Physics*, 8th ed. (Wiley, Hoboken, NJ, 2005).

[5] Y. Tserkovnyak, A. Brataas, and G. E. W. Bauer, Phys. Rev. Lett. **88**, 117601 (2002).

[6] K. Uchida, J. Xiao, H. Adachi, J. Ohe, S. Takahashi, J. Ieda, T. Ota, Y. Kajiwara, H. Umezawa, H. Kawai, G. E. W. Bauer, S. Maekawa, and E. Saitoh, Nat. Mater. **9**, 894 (2010).

[7] L. J. Cornelissen, J. Liu, R. A. Duine, J. B. Youssef, and B. J. van Wees, Nat. Phys. **11**, 1022 (2015).

[8] S. Das, A. Ross, X. X. Ma, S. Becker, C. Schmitt, F. van Duijn, E. F. Galindez-Ruales, F. Fuhrmann, M.-A. Syskaki, U. Ebels, V. Baltz, A.-L. Barra, H. Y. Chen, G. Jakob, S. X. Cao, J. Sinova, O. Gomonay, R. Lebrun, and M. Kläui, Nat. Commun. **13**, 6140 (2022).

[9] C. Hahn, G. de Loubens, O. Klein, M. Viret, V. V. Naletov, and J. Ben Youssef, Phys. Rev. B **87**, 174417 (2013).

[10] R. Lebrun, A. Ross, O. Gomonay, S. A. Bender, L. Baldrati, F. Kronast, A. Qaiumzadeh, J. Sinova, A. Brataas, R. A. Duine, and M. Kläui, Commun. Phys. **2**, 50 (2019).

[11] T. Wimmer, A. Kamra, J. Gückelhorn, M. Opel, S. Geprägs, R. Gross, H. Huebl, and M. Althammer, Phys. Rev. Lett. **125**, 247204 (2020).

[12] X.-Y. Wei, O. A. Santos, C. H. S. Lusero, G. E. W. Bauer, J. Ben Youssef, and B. J. van Wees, Nat. Mater. **21**, 1352 (2022).

[13] S. M. Rezende, R. L. Rodríguez-Suárez, and A. Azevedo, Phys. Rev. B **93**, 014425 (2016).

[14] T. Liu, J. Peiro, D. K. de Wal, J. C. Leutenantsmeyer, M. H. D. Guimarães, and B. J. van Wees, Phys. Rev. B **101**, 205407 (2020).

[15] W. Xing, L. Qiu, X. Wang, Y. Yao, Y. Ma, R. Cai, S. Jia, X. C. Xie, and W. Han, Phys. Rev. X **9**, 011026 (2019).

[16] D. MacNeill, J. T. Hou, D. R. Klein, P. Zhang, P. Jarillo-Herrero, and L. Liu, Phys. Rev. Lett. **123**, 047204 (2019).

[17] H. Nakayama, M. Althammer, Y.-T. Chen, K. Uchida, Y. Kajiwara, D. Kikuchi, T. Ohtani, S. Geprägs, M. Opel, S. Takahashi, R. Gross, G. E. W. Bauer, S. T. B. Goennenwein, and E. Saitoh, Phys. Rev. Lett. **110**, 206601 (2013).

[18] R. Wu, A. Ross, S. Ding, Y. Peng, F. He, Y. Ren, R. Lebrun, Y. Wu, Z. Wang, J. Yang, A. Brataas, and M. Kläui, Phys. Rev. Appl. **17**, 064038 (2022).

[19] F. Feringa, G. E. W. Bauer, and B. J. van Wees, Phys. Rev. B **105**, 214408 (2022).

[20] Y. Peng, S. Ding, M. Cheng, Q. Hu, J. Yang, F. Wang, M. Xue, Z. Liu, Z. Lin, M. Avdeev, Y. Hou, W. Yang, Y. Zheng, and J. Yang, Adv. Mater. **32**, 2001200 (2020).

[21] S. Calder, A. V. Haglund, Y. Liu, D. M. Pajerowski, H. B. Cao, T. J. Williams, V. O. Garlea, and D. Mandrus, Phys. Rev. B **102**, 024408 (2020).

[22] See Supplemental Material at http://link.aps.org/supplemental/10.1103/PhysRevB.107.L180403 for the atomic force microscopy measurements on device D1; temperature dependence of $R_{nl}^{(1\omega)}$ on device D3; local measurements $R_{l}^{(1\omega)}$ in comparison to measurements on Pt strips directly on SiO_2 to exclude Hanle magnetoresistance; electrical characterization of exfoliated CrPS4; magnetic characterization of bulk CrPS4; distance dependence of $R_{nl}^{(1\omega)}$ for different temperatures, complementing Fig. 5; and second harmonic measurements in the local and nonlocal Pt strips. The Supplemental Material also contains Refs. [7,20,23].

[23] S. Vélez, V. N. Golovach, A. Bedoya-Pinto, M. Isasa, E. Sagasta, M. Abadia, C. Rogero, L. E. Hueso, F. S. Bergeret, and F. Casanova, Phys. Rev. Lett. **116**, 016603 (2016).

[24] F. L. Bakker, A. Slachter, J.-P. Adam, and B. J. van Wees, Phys. Rev. Lett. **105**, 136601 (2010).

[25] W. Zhu, C. Song, L. Han, H. Bai, Q. Wang, S. Yin, L. Huang, T. Chen, and F. Pan, Adv. Funct. Mater. **32**, 2108953 (2022).

[26] K. Oyanagi, J. M. Gomez-Perez, X.-P. Zhang, T. Kikkawa, Y. Chen, E. Sagasta, A. Chuvilin, L. E. Hueso, V. N. Golovach, F. S. Bergeret, F. Casanova, and E. Saitoh, Phys. Rev. B **104**, 134428 (2021).

[27] L. J. Cornelissen, J. Shan, and B. J. van Wees, Phys. Rev. B **94**, 180402(R) (2016).

[28] L. J. Cornelissen, K. J. H. Peters, G. E. W. Bauer, R. A. Duine, and B. J. van Wees, Phys. Rev. B **94**, 014412 (2016).

[29] A. G. Gurevich and G. A. Melkov, *Magnetization Oscillations and Waves* (CRC Press, Boca Raton, 1996).

[30] P. Tang and G. E. W. Bauer (unpublished).